Hot Corrosion Behavior of 304 & P91 Graded Composition Transition Joint under Molten Sulfate Salts

Ting Sun[1], Shanshan Hu[1*], Alexander I. Ikeuba[1], Yuying Wen[1], Xingru Tan[1], Youyuan Zhang[1], Haiyang Qian[4], Yanli Wang[2], Zhili Feng[2], Bai Cui[3], Xingbo Liu[1*]

1 Mechanical & Aerospace Engineering Department, Benjamin M. Statler College of Engineering and Mineral Resources, West Virginia University, Morgantown, WV 26505, USA

2 Metals and Ceramics Division, Oak Ridge National Laboratory, Oak Ridge, TN 37831, USA

3 Department of Mechanical and Materials Engineering, University of Nebraska-Lincoln, Lincoln, Nebraska 68588, USA

4. GE Gas Power, GE Vernova, 200 Great Pond Dr, Windsor, CT 06095, USA

Corresponding authors, email: shanshan.hu@mail.wvu.edu (Shanshan Hu), Xingbo.liu@mail.wvu.edu (Xingbo Liu)

Abstract

A novel graded composition transition joint (GCTJ) between AISI 304 stainless steel and ASTM A335 P91 steel, has been demonstrated remarkablely superior creep performance compared to the conventional dissimilar metal weldment (DMW) under equivalent conditions. However, this advance is challenged by hot corrosion under salt deposition at elevated temperatures. This study investigates the hot corrosion behavior of 304&P91 GCTJ exposed to sulfate salts at 700°C. Compared to the 304 steel, corrosion attacks initiate in the P91 triangle, where the dual-phase microstructure of ferrite and tempered martensite significantly influences pitting initiation. Anodic dissolution mainly occurs within the tempered martensite due to more vulnerable sites within the tempered martensite. With prolonged exposure, corrosion propagates across both phases, and the corrosion depth within the P91 triangle is related to the exposed surface area ratio between 304 and P91. Electrochemical analysis reveals the occurrence of galvanic corrosion between the 304 and P91, with a positive linear relationship between anodic dissolution current density (I_a) and the exposed surface area ratio between 304 and P91 in molten salts, further emphasizing the critical impact of this ratio on the corrosion severity in the P91

triangle. These findings underscore the importance of transition zone design optimization in mitigating localized corrosion.

Key Words: Transition joint; Galvanic corrosion; Molten salts; Microstructure

1. Introduction

In the construction of boiler systems, AISI 304 stainless steel is selected for superheated tubes because of its superior oxidation resistance while ASTM A335 P91 steel is used for steam headers due to its exceptional strength and cost-effectiveness[1–3]. Consequently, welding of these dissimilar metals within the boiler infrastructure becomes inevitable to meet operational demands and reduce manufacturing cost [4–6]. However, this dissimilar metal weldment (DMW) is susceptible to creep cavities under high temperatures and pressures, leading to premature failure compared to either base metal [7,8]. Besides, the distinct mismatch of the coefficient of thermal expansion (CTE) at the dissimilar interface results in strain concentration, accelerating the service failure of DMWs [9,10].

In a bid to address these challenges, we developed a novel graded composition transition joint (GCTJ) incorporating P91 and 304 [11]. The computational simulation and experimental test indicate that stress accumulation in the transition zone is significantly reduced compared to conventional DMWs under equivalent conditions, thereby providing enhanced creep resistance [12]. Different from conventional graded transition joints printed by controlling the ratio of varying alloy powders in a molten pool [13], this GCTJ with a graded composition from 100% P91 to 100% 304, is achieved through the seamless fusion of two alloy ridges in the transition zone. This design effectively minimizes the formation of undesirable phases that arise from the complete fusion of mixed alloy powders, which could impair the creep performance [13–15]. Therefore, the GCTJ represents a promising solution for improving the reliability of dissimilar metal connections in the advanced ultra-supercritical (A-USC) power plant.

Despite these advancements in the transition joint, hot corrosion also plays an important role in the premature failure of joints under service conditions[16,17]. The corrosion is induced by the formation of a molten layer with the deposition of corrosive salts [18,19], such as Na_2SO_4, $MgSO_4$, V_2O_5, and NaCl, from combustion gases onto tube surfaces. The

molten layer acts as an ion conductor, inducing electrochemical corrosion on the GCTJ surface. Additionally, the inherent potential difference due to compositional heterogeneity at the dissimilar metal interface poses a risk of galvanic corrosion, further accelerating the degradation of GCTJ. In galvanic coupling, the metal with lower corrosion resistance (i.e., more negative corrosion potential) functions as an anode. For instance, in the P91&304 coupling, P91 serves as an anode suffering much more severe corrosion attacks compared to the intrinsic corrosion that happens on the base metal zone of each alloy [20–22]. This nonuniform corrosion on the joints could trigger localized degradation, leading to stress concentration and microcrack initiation under these defects [23,24].

Thus, it is imperative to investigate the hot corrosion behavior of these novel transition joints. The novel 304&P91 GCTJ was produced using laser powder bed fusion (LPBF) and hot isostatic pressing (HIP) followed by heat treatment. To assess the hot corrosion behavior of the 304&P91 joint for use in the next-generation boiler for the A-USC power plant, the hot corrosion test was conducted under a simulated salt mixture (50at% Na_2SO_4 and 50at% $MgSO_4$) at 700°C. In this study, the microstructure of pristine and corroded GCTJ as well as the high-temperature electrochemical characteristics were examined. Particular attention was given to the corrosion feature of the vulnerable P91 steel within the transition zone. The effect of the dual phase on the corrosion initiation across the P91 triangle is investigated by optical microscope (OM), scanning electron microscopy (SEM) coupled with energy dispersive spectroscopy (EDS), electron backscatter diffraction (EBSD), and scanning kelvin probe force microscopy (SKPFM). The macro galvanic effects were assessed through a series of electrochemical tests conducted at 700°C. This paper aims to provide a preliminary understanding of the corrosion behavior of GCTJ, offering insights to mitigate the impact of corrosion degradation on service performance, and thereby improving the design and manufacturing process of new transition joints.

2. Experiments

2.1 Materials

The novel 304&P91 GCTJ was produced using laser powder bed fusion (LPBF) and hot isostatic pressing (HIP) followed by heat treatment, as shown in Fig. S1a. In contrast, the conventional dissimilar metal weld (DMW) was produced by welding cast 304 and P91

base metals with ER309 filler material. The configurations of both joints are shown in Fig. 1. The joint samples and the base samples were machined via electro-discharge machining (EDM) for hot corrosion testing, microstructural analysis, and electrochemical measurements. To minimize the effects of as-received surface roughness on corrosion behavior of joints, all surfaces of testing specimens were carefully ground with 180 to 4000 grit silicon carbide paper and then gradually mirror polished with 1 μm and 0.05 μm colloidal silica suspension. This uniform, polished finish is critical for reducing variability from surface irregularities and for enabling clear observation of initial pitting corrosion. Finally, the specimens underwent ultrasonic cleaning in ethyl alcohol and were dried with compressed air to eliminate potential contaminants. The chemical compositions of 304 and P91 are provided in Table *1*.

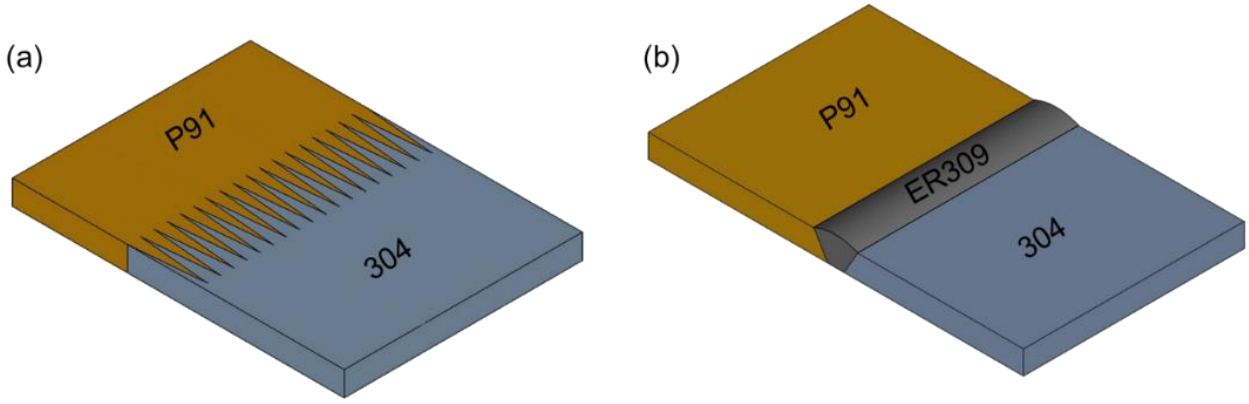

Fig. 1 The schematic of the 304&P91 joint configuration: (a) GCTJ and (b) DMW.

Table 1 The chemical composition of 304 and P91.

Content (wt%)	Fe	C	Si	Ni	Mn	Cr	Mo	V	Nb
P91	Balance	0.08	0.41	0.06	0.47	9.01	0.93	0.18	0.07
304	Balance	0.028	0.66	9.20	1.20	18.40	---	---	---

2.2 Hot corrosion test under applied salts

The hot corrosion test was conducted under a deposited salt mixture (50at% Na_2SO_4 and 50at% $MgSO_4$) at 700°C. The salt mixture was first dissolved in deionized water to create

a homogenous solution. This solution was then uniformly applied to the pre-heated surfaces of the joint coupons using an airbrushing technique, ensuring consistent coverage across all specimens [25]. Multiple passes of the airbrush were employed to achieve the desired deposition amount. Following the application, the coated specimens were subjected to a drying process at 300 °C for several hours to effectively remove any residual moisture, thereby promoting the formation of a stable and adherent salt layer. To monitor and control the amount of salt deposited, the specimens were weighed prior to the deposition process to establish a baseline (bare metal weight). Subsequent weighing was performed after every five spray cycles to track the incremental increase in salt loading. This iterative process continued until the target deposition amount of 10 ± 0.5 mg cm^{-2} was achieved. The chosen deposition quantity was informed by existing literature and preliminary experimental data, which indicated that this specific amount facilitates the formation of a reproducible and well-adhered salt layer conducive to consistent corrosion testing. Fig. S2 illustrates the relatively uniform salt layer achieved following this procedure. The hot corrosion test for joint coupons was performed at 700°C in ambient air for 10 min, 30 min, 1 h and 5 h, during which the salt mixture remained fully molten, as confirmed by DSC data (Fig. S3).

2.3 Microstructural characterization

The P91 region of both joint specimens was chemically etched by Villela reagent (1 g picric acid + 5 mL HCl + 100 mL ethanol), while the 304 region was electrochemically etched in a 10% oxalic acid solution. The pristine microstructure of the transition zone was examined by OM, SEM/EDS and EBSD. After the corrosion tests, the corrosion products, along with salt residues, were characterized by X-ray diffraction (XRD) and SEM/EDS. To assess the corrosion morphology across the transition zone, the corroded surfaces were initially rinsed with hot water to remove loosely adherent deposits; however, the more strongly adhered corrosion products persisted even after several hours of washing [26]. In order to further remove the adhered corrosion products, GCTJ and DMW with the same corrosion time were mounted together and gently ground using a standardized procedure employing 2500 and 4000 grit silicon carbide paper, respectively, at a fixed rotational speed for 1 minute. The specimens were then polished for 3 min, ultrasonically cleaned and dried. Finally, the corrosion depth on the P91 region of both

joint specimens was measured using a 3D optical microscope. Although this procedure may compromise the precise quantification of pit depth, it is essential for the comprehensive evaluation of degradation morphology and progression across the entire transition zone.

2.4 Scanning Kelvin probe force microscopy measurement

The scanning Kelvin probe force microscopy (SKPFM) measurements were performed on the GCTJ sample using an Asylum Research Atomic Force Microscopy (AFM, MFP-3D Origin, Oxford Instruments) under ambient conditions. A conductive Pt/Ir-coated silicon tip with a resonant frequency of 45–95 kHz was employed for probing. The Volta potential was mapped across an 80 x 80 μm area at a scanning rate of 0.5 Hz, achieving a resolution of 256 x 256 pixels. SKPFM operated in a two-pass mode: the first pass acquired the topographic image of the sample, while in the second pass, the Volta potential was acquired by elevating the cantilever 300 nm above the surface with a bias of 3 V applied at the probe tip.

2.5 Electrochemical test

The experiments were conducted in a vertical tube furnace under an ambient atmosphere. All electrochemical tests were performed using the Gamry reference 600 potentiostat, in a typical three-electrode system. The electrodes were connected to a tungsten wire by electric welding and then sealed in an alumina tube. A Pt wire with a diameter of 0.6 mm was used as a reference electrode (RE). For the polarization experiments, P91 or 304 acted as working electrodes (WE) with a Pt wire as the counter electrode (CE). The exposure of molten salts was controlled on a specified area of the WE surface using ceramic glue. The distance between the RE and WE was maintained at 3 mm. The alumina crucible with enough salt mixture was heated to 700^{o}C and held for 4 h to make the salts fully molten. After that, the as-made electrode probe was hung above the salts and slowly dropped into the molten salts. The open circuit potential (OCP) curve was recorded after immersion. The potentiodynamic polarization (PDP) curve of 304 or P91 was recorded once the OCP became stable. The potentiodynamic polarization curves were measured at a potential scan rate of 1 mV/s. For the galvanic corrosion measurements, 304 and P91 steel were connected as WE1 and WE2 to the Gamry

potentiostat. The galvanic current density and galvanic potential between 304 and P91 were monitored by the zero resistance ammeter (ZRA) technique. A ZRA technique is a current-to-voltage converter that produces a voltage output proportional to the current flowing between its two input terminals while imposing a 'zero' voltage drop to the external circuit. In the corrosion test, a ZRA is typically used to measure the galvanic coupling current between two dissimilar electrodes.

3. Results

3.1 Microstructural characterization

The microstructure of the 304&P91 GCTJ is shown in Fig. 2. As seen in Fig. 2a, there are three different zones on the surface along the y-axis, i.e., P91 base metal, triangle-featured transition zone, and 304 base metal. Within the transition zone, the P91 and 304 are seamlessly joined together by the fusion of isosceles triangle-shaped alloys. These triangles are 9 mm in height and 5.2 mm in base length. Along the y-axis, the composition of P91 gradually decreases, presenting an increasing exposed surface area ratio between 304 and P91. The zooming-in of different portions of GCTJ, including the interface, base metals, and the transition zone, is provided in Fig. 2b to Fig. 2i. The whole GCTJ is totally dense and no voids are found along the interface (Fig. 2b), indicating good bonding between P91 and 304. The 304 base metal is composed of austenite with some twins shown in Fig. 2c and P91 base metal consists of tempered martensite shown in Fig. 2d. It is noteworthy that the microstructure of 304 and P91 in the transition zone differs from the base metal. As shown in Fig. 2e and f, the austenite twins disappear in the 304 triangles. In the P91 triangles, there are distinct dual phases, i.e., the smooth phase and precipitation-decorated tempered martensite (Fig. 2h and i). The metallography of the smooth phase is consistent with ferrite, reported in prior findings [27,28]. Microhardness measurements validate this identification, showing that the ferrite phase exhibits a microhardness of approximately 15.8 $HV_{0.025}$ lower than that of tempered martensite [29–31], as depicted in Fig. S4. The ratio between ferrite and P91 matrix has an increasing trend along the y-axis due to the geometry of the transition zone, as shown in Fig. 2g to Fig. 2i.

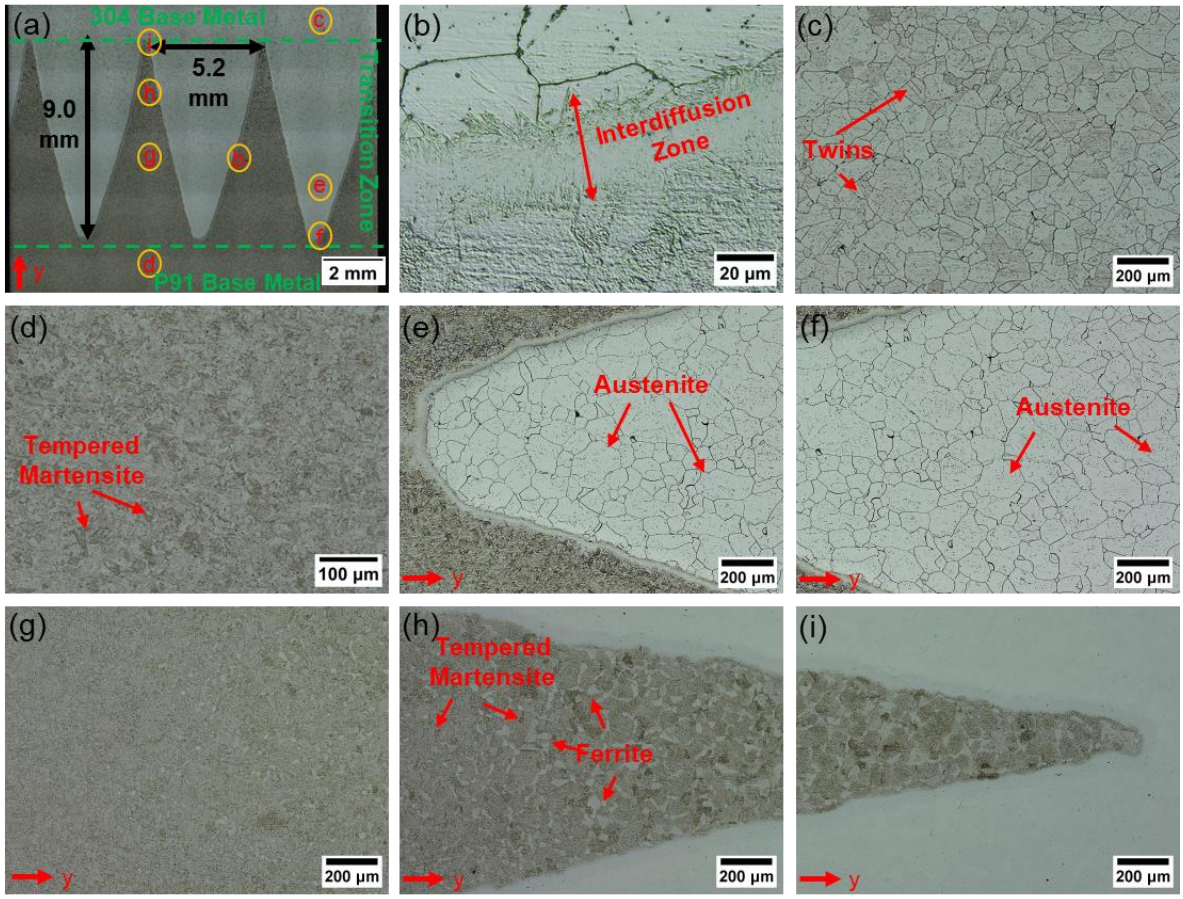

Fig. 2 The optical microstructures of 304&P91 GCTJ: (a) Overview of the GCTJ, showing P91 base metal, transition zone, and 304 base metal along the y-axis; (b) The interdiffusion zone between 304 and P91 without any voids, indicating a good bonding at the dissimilar interface; (c) Microstructure of the 304 base metal; (d) Microstructure of the P91 base metal; (e) and (f) Electrochemically polished 304 triangle in the transition zone; (g), (h) and (i) Partially etched P91 triangle, representing the bottom, middle, and top regions, respectively, with distinct dual-phase feature.

To elucidate the dual-phase microstructure, 2D EBSD measurements were performed on the P91 triangle zone. The band contrast (BC) maps, shown in Fig. 3a and Fig. 3b, reveal that tempered martensite with lower BC values appears darker compared to ferrite [32]. The corresponding kernel average misorientation (KAM) map for the same areas is shown in Fig. 3c and Fig. 3d. The highest KAM values are found within tempered martensite, indicating that the higher lattice distortion concentrates in the tempered martensite. This result is consistent with the previous results, in which the formation of dislocation pile-up within the tempered martensite was attributed to the martensitic transformation stresses [32,33].

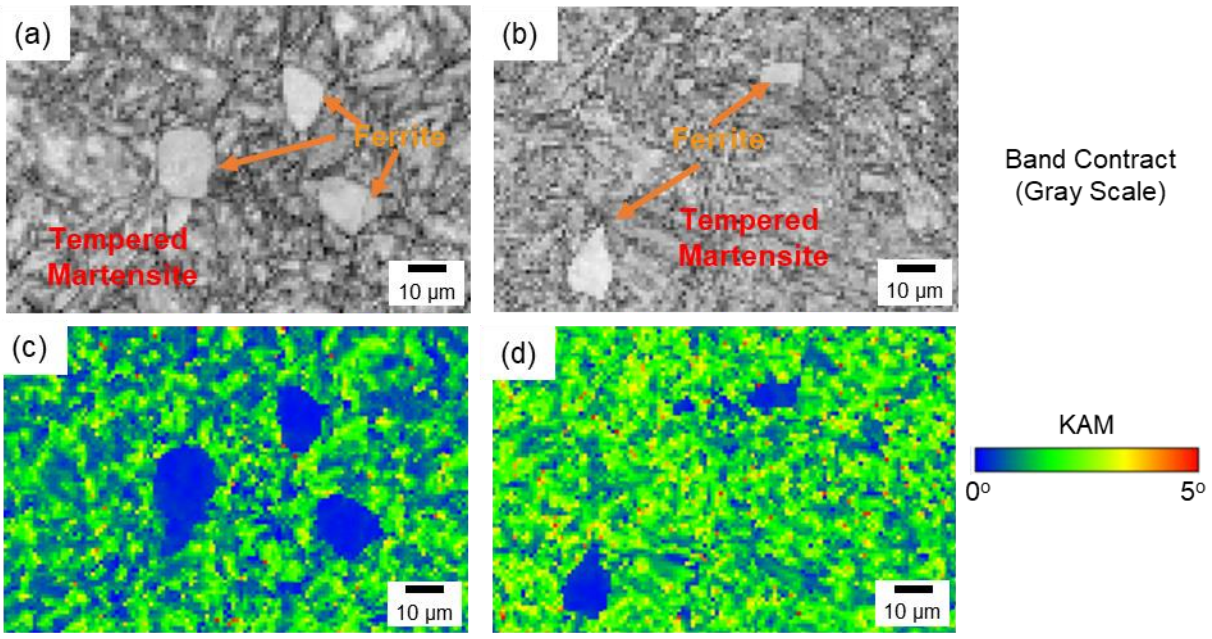

Fig. 3 EBSD result of the selected zone within the P91 triangle: (a) and (b) The band contrast (BC) map; (c) and (d) The kernel average misorientation (KAM) map in the P91 triangle zone.

3.2 Initial Corrosion Feature of the P91 triangle

The surface morphology of GCTJ after 10 min of corrosion is presented in Fig. S5. Early-stage corrosion predominantly appears as pitting on the more susceptible P91 side, with minimal damage observed on the 304 side. These initial corrosion pits with diameters of 1-5 μm are observed at the ferrite-tempered martensite phase boundaries, indicated by red circles as shown in Fig. 4a and Fig. 4b. By prolonging the corrosion exposure to 30 min, the corrosion spreads across the P91 triangle, with pits expanding into irregular shapes with widths of 10-60 μm, as shown in Fig. S6. The preferential pitting behavior is further clarified by overlaying the pre-exposure microstructure with the post-corrosion surface. As depicted in Fig. 4c, the navy-colored pits predominantly localize within the tempered martensite matrix and near the orange ferrite phase, suggesting that tempered martensite is more prone to corrosion than ferrite.

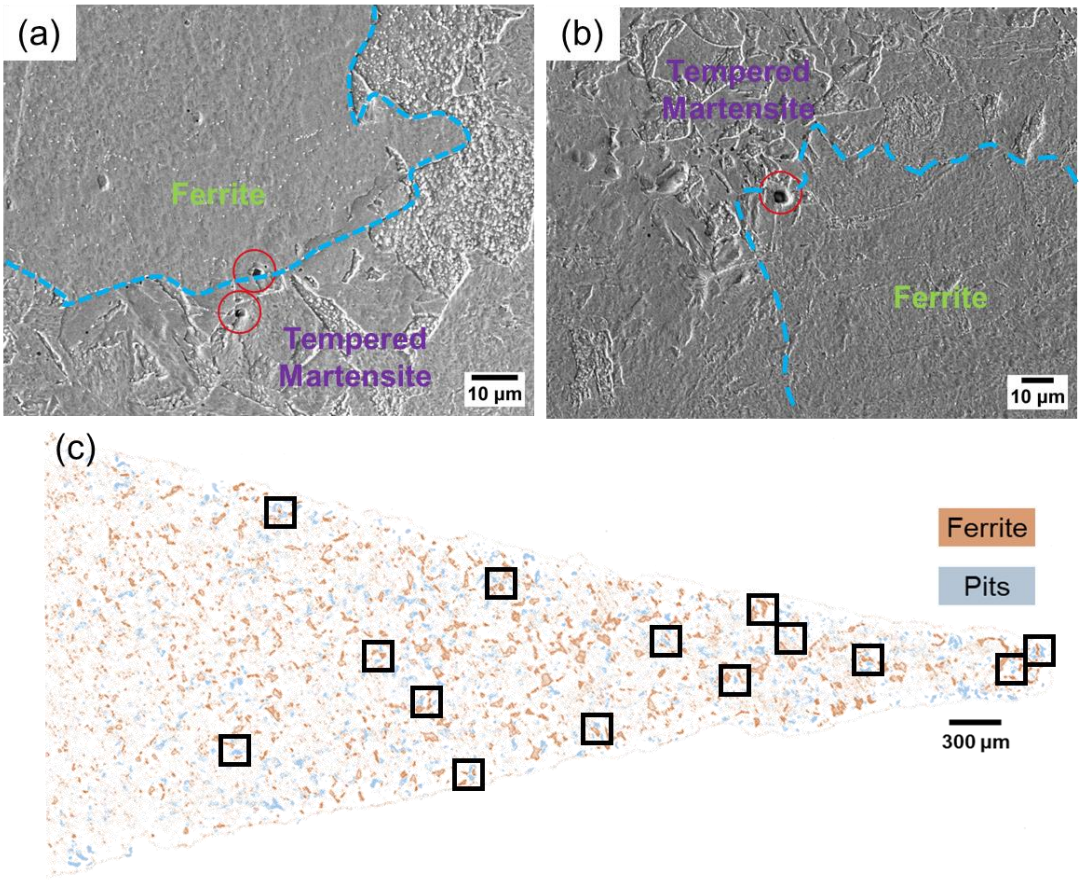

Fig. 4 The SEM of the corroded P91 triangle after 10 min in (a) and (b), with blue dashed lines indicating the phase boundaries between tempered martensite and ferrite. The overlaid OM figures of the microstructure before corrosion and pits after 0.5 h corrosion in (c). The ferrite phase, extracted from the original P91 triangle microstructure, and the pits from the 0.5 h corroded surface of the same P91 triangle are highlighted.

To elucidate the electrochemical properties of these two phases within the GCTJ, the Volta potential, which correlates with the surface work function of each phase, was measured using SKPFM [34]. Based on the morphology features presented in Fig. 2, tempered martensite and ferrite are distinctly identified in the topographic map (Fig. 5a). The corresponding Volta potential map (Fig. 5b) illustrates the distribution of surface potentials, where regions with higher potential are considered more noble, while those with lower potential are more prone to corrosion [35,36]. As shown in Fig. 5b, ferrite displays a relatively uniform Volta potential, whereas tempered martensite exhibits significant variations. The variations of Volta potential are further detailed through line scans across tempered martensite and ferrite, as shown in Fig. 5c and Fig. 5d. Within tempered

martensite, the largest Volta potential differences are recorded at around 100 mV. This phenomenon has been observed and attributed to carbide precipitation, where areas of higher potential correspond to carbides while the surrounding areas with lower potential are identified as corrosion initiation sites [33]. Despite these local variations, the average Volta potentials between ferrite (141.98 mV) and tempered martensite (140.34 mV) are comparable, suggesting that the overall corrosion resistance of both phases is similar.

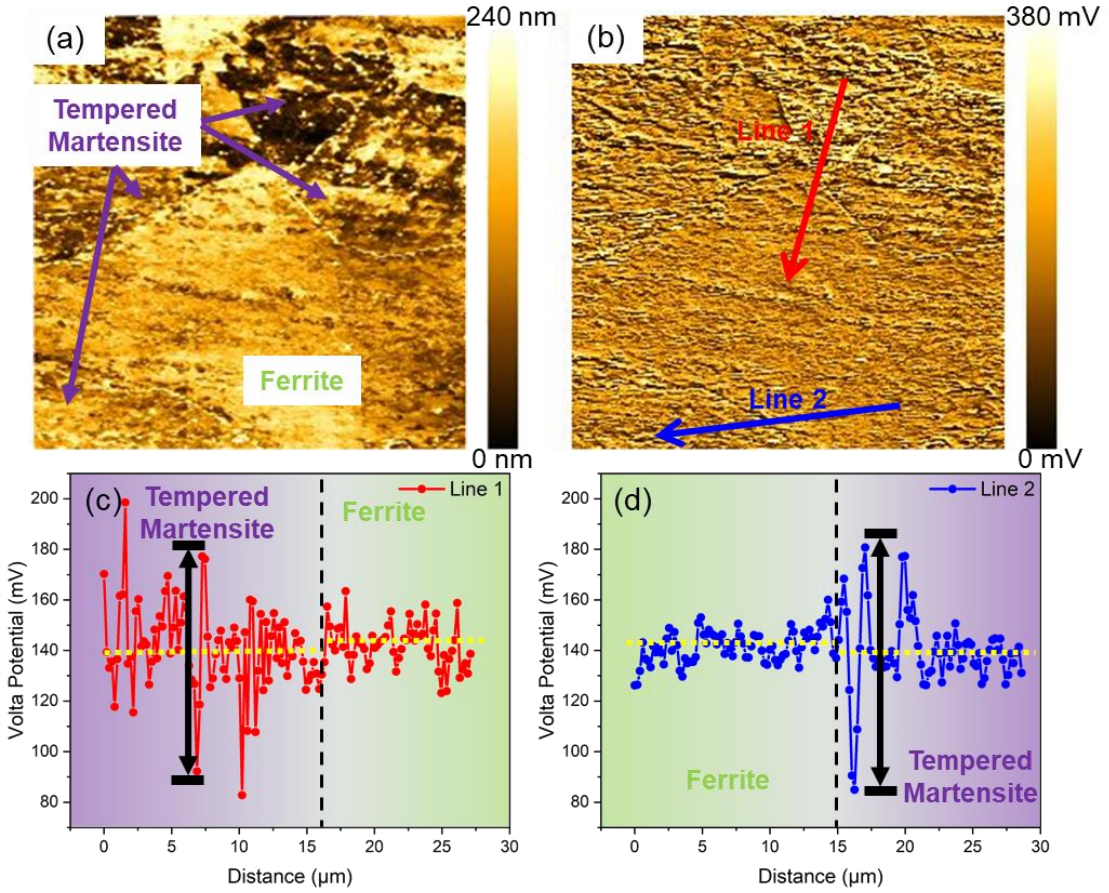

Fig. 5 The SKPFM maps of GCTJ: (a) Topographic image; (b) Corresponding Volta potential distribution; (c) Line scan result of Volta potential of Line 1 and (d) line scan result of Volta potential of Line 2. Black arrows in (c) and (d) indicate pronounced Volta potential fluctuations (~100 mV) within the tempered martensite phase. The yellow dashed lines represent the average Volta potentials for ferrite and tempered martensite.

3.3 Prolonged Corrosion Test

The morphology of the exposed transition zone of GCTJ after 1 h and 5 h corrosion tests is present in Fig. 6a and Fig. 6b, respectively. On the 304 side, residual salts and brass-

colored corrosion products are loose and easily detached. In contrast, on the P91 side, the darker corrosion products are firmly adhered to the matrix. The XRD results of the 304 base and P91 base are shown in Fig. 6c, show that both P91 and 304 are covered with residual eutectic salts ($Na_3Fe(SO_4)_3$ and $Na_6Mg(SO_4)_4$), iron oxides (Fe_2O_3 and Fe_3O_4), magnesium oxides (MgO) and chromium sulfide (CrS). The localized dissolution of Fe and Cr is found on the surface of bare 304 metal, shown in Fig. 6d, Fig. 6g and Fig. 6h. For P91 metal, the top triangle zone is covered by a large number of wire-like Fe_2O_3 in rusty red (Fig. 6b, Fig. 6e and Fig. 6j). MgO is found above these oxidized hills, as shown in Fig. 6i. The P91 bottom triangle zone is covered by Fe-dissolved residual salts and Fe_3O_4 in a dark color, as shown in Fig. 6f, Fig. 6k and Fig. 6l.

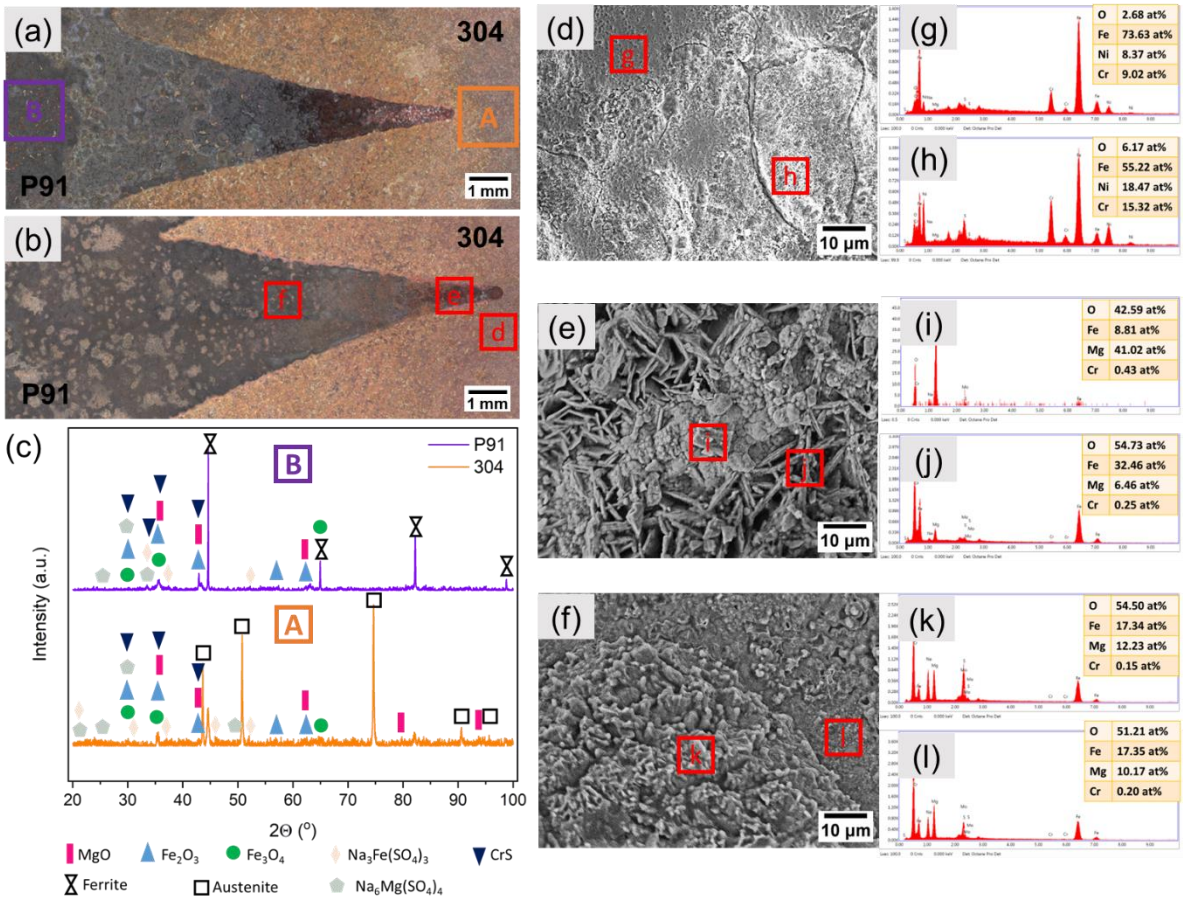

Fig. 6 The corroded surface of GCTJ (a) after 1 h and (b) after 5 h; (c) The XRD of 304 base zone (A in Fig. 6a) in and P91 base zone (B in Fig. 6a) after 1 h corrosion with residual salts; (d) The SEM image of localized corrosion morphology of 304 base metal; (e) The rusty red P91 top triangle zone; (f) the black P91

bottom triangle zone after 5 h corrosion; (g-l) The elemental content of surface corrosion products by EDS in different positions.

The corroded depth of joints is depicted in Fig. 7 and Fig. 8. After 1 h exposure, the corrosion on the P91 triangle is significantly more severe while the 304 triangle appears smooth and free of visible corrosion pits after re-polishing, as shown in Fig. 7a. The corrosion on the P91 triangle is non-uniform, presenting a gradient severity across the whole P91 triangle. The pitting depth of various locations within the P91 triangle, along the center and interface of the P91 triangle, was measured using a 3D optical microscope. The pitting depth of various locations within the P91 triangle, along the center and interface of the P91 triangle, was measured using a 3D optical microscope. Localized optical microscopy images along the center (Fig. 7b, Fig. 7c, Fig. 7e, and Fig. 7g) and interface (Fig. 7b, Fig. 7d, Fig. 7f, and Fig. 7h) of the P91 triangle reveals a distinct gradient in corrosion depth within the P91 triangular region along the y-axis. Specifically, regions of the P91 triangle that are adjacent to a higher exposed surface area of 304 tend to develop deeper corrosion pits. Most isolated pits are within the P91 triangle, while the deepest pits, approximately 10 μm, develop into ditches at the front of the P91 triangle interface (Fig. 7d).

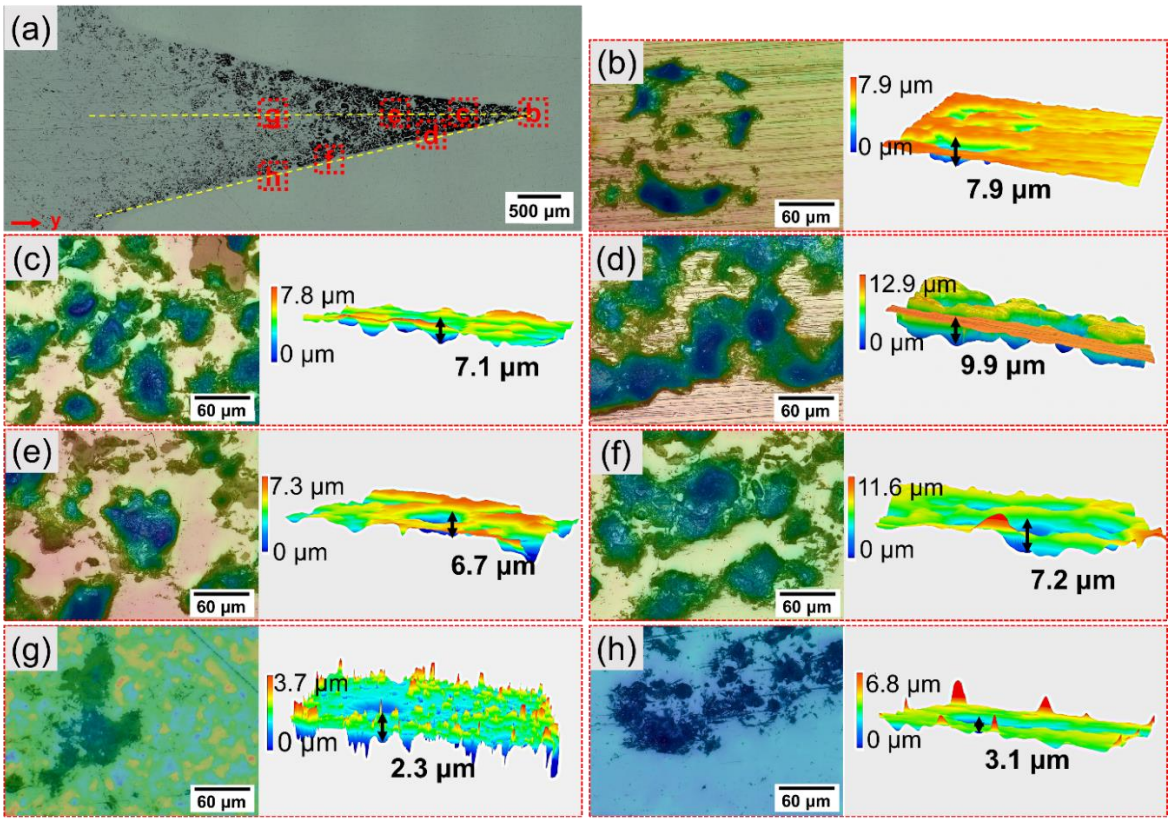

Fig. 7 The morphology of corroded GCTJ after 1 h corrosion: (a) Overview of the transition zone surface. The yellow dashed lines mark the center and the interface of the P91 triangle. (b) to (h) The degradation depth of different positions along the center and interface of the P91 triangle.

After 5 h of corrosion, minor pits with inconspicuous depth are present on the 304 side (Fig. S7). A gradient in corrosion severity persists within the P91 triangle, as shown in Fig. 8a. The corrosion depth within the P91 triangle increases along the y-axis which corresponds to the region with less P91 exposed surface area. Pitting corrosion is evident at the tip of the P91 triangle, with a depth of 21.5 μm (Fig. 8b), while the upper-middle region undergoes more extensive corrosion, with degradation depths ranging from 24 to 42 μm (Fig. 8c and Fig. 8d). The ditch-like corrosion predominates in the bottom-middle zone, with depths between 5 and 28 μm (Fig. 8e to Fig. 8h). The P91 bottom triangle zone exhibits the least corrosion depth compared to the other areas (Fig. 8i and Fig. 8j).

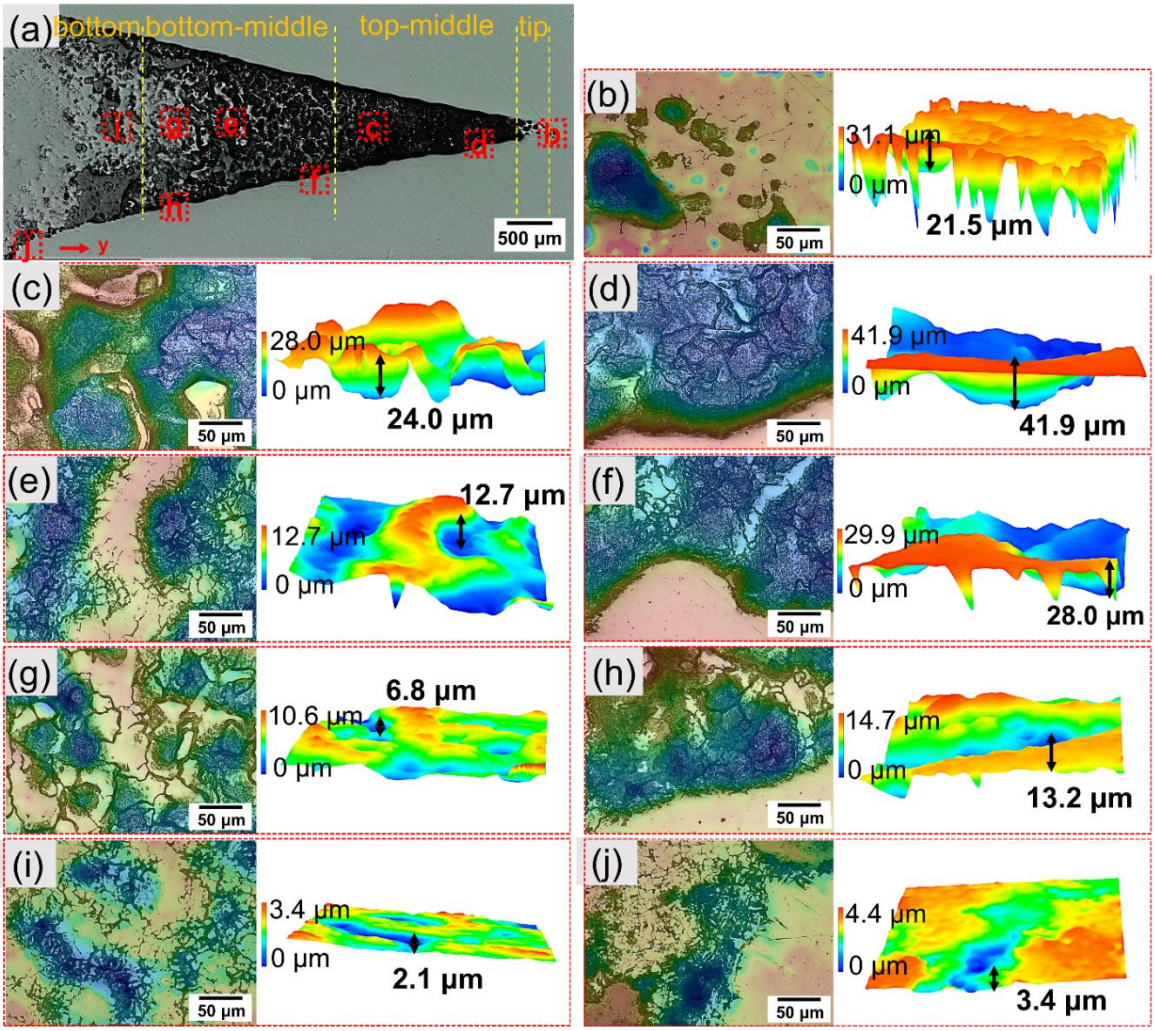

Fig. 8 The morphology of corroded GCTJ after 5 h corrosion: (a) Overview of the transition zone surface, revealing four distinct regions along the y-axis, each with different corrosion characteristics. (b) to (j) The degradation depth of different positions on the P91 triangle.

The elemental mapping of a cross-section of isolated pits on the P91 triangle after 1 h corrosion test (about 3 mm from the P91 triangle tip along the central line) is presented in Fig. 9a. Residual magnesium and sodium are present on the top surface, and the outermost corrosion products are predominantly composed of iron oxides. Notably, sulfur has penetrated into the substrate, leading to the formation of chromium sulfide at the bottom of the corrosion pits. This sulfide formation, even after short-term corrosion exposure, implies significant outward diffusion of chromium from the matrix, resulting in localized Cr depletion beneath the sulfides (as shown in Fig. S8) [37,38]. The cross-section of 5 h exposed GCTJ is presented in Fig. 9b. The corrosion depth on the 304 side is much

shallower than that in the P91 triangle. Along the central line of the P91 triangle, the corrosion depth increases from 4.4 μm at the bottom zone to 44.0 μm at the top zone.

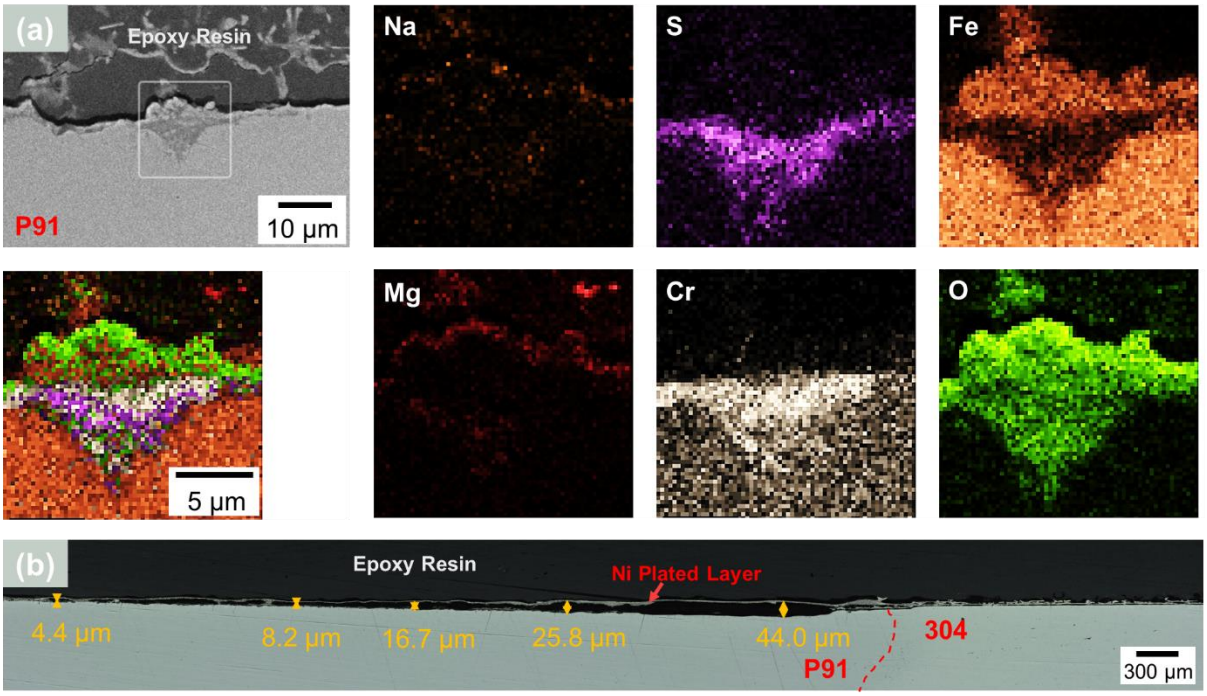

Fig. 9 (a) The EDS of a cross-section of pits on the P91 triangle after a 1 h corrosion test; (b) The whole cross-section of the P91 triangle after a 5 h corrosion test.

3.4 Electrochemical test

To investigate the factors driving the observed corrosion behavior, a series of electrochemical experiments were performed using electrode couples with identical areas of P91 and 304. Fig. 10a shows the change of OCP of both P91 and 304 in molten 50 at% Na_2SO_4+50 at% $MgSO_4$ salt at 700°C. Both OCPs show the same trend: the initial drop then increase followed the stable stage in OCP. The initial drop in the OCP ascribed to the dissolution of the thin oxide layer which is formed when slowly immersing the electrodes into the molten salts [39]. The subsequent rapid increase in the OCP infer that the spontancous growth of the oxide [40]. After about half an hour, the stable OCP of 304 (-0.09 V vs. Pt) is about 0.11 V higher than that of P91(-0.20 V vs. Pt), indicating that galvanic corrosion of 304 and P91 can occur readily in high-temperature molten sulfate salts [41]. The 304 with the more positive potential acts as the cathode in the galvanic couple, while P91 acts as the anode, as shown in Fig. 10b. The kinetic parameters,

including anodic and cathodic Tafel constants (β_a and β_c, respectively), for P91 and 304 in molten salts, and the galvanic current density (I_g) and the galvanic potential (E_g), are shown in Table 2**.** The corrosion potential of 304 is higher than that of P91, indicating that P91 is more vulnerable to hot corrosion attacks. The intersection between the cathodic branch of 304 and the anodic branch of P91 shows that the galvanic corrosion current density is about 112 μA cm^{-2} with a galvanic potential of -0.16 V vs. Pt. This indicates that in the P91/304 galvanic couple, P91 would serve as an anode which is in the active dissolution state while 304 will serve as the cathode with high tendency towards passivation.

The steady-state I_g and potential of the P91/304 couple in the molten salts are recorded and plotted as a function of time, as shown in Fig. 10d. It is important that the I_g is a “net” current density that represents the difference between the local anodic current and the local cathodic current on the electrode [41]. Thus, the positive I_g between 304 and P91 of equal area indicates the activity of anodic reactions on the P91 electrode is higher than that on the 304 electrode. An initial I_g can reach 500 μA cm^{-2}, meaning vigorous dissolution happens on the P91 electrode. After 1.5 h, the stable I_g between P91 (anode) and 304 (cathode) is about 100 μA cm^{-2}. A detailed 90 s portion of Fig. 10d at 6400 s after immersion is shown in Fig. 10c. The pronounced downward potential pulses correspond to dissolution events during the experiment, with the associated upward and downward current pulses reflecting the dissolution of P91 and 304, respectively. This indicates that hot corrosion occurs on both alloys simultaneously. However, as noted, the overall positive I_g suggests that P91 predominantly acts as the anode during the galvanic corrosion, consistent with microscopic observations showing severe corrosion on P91 and minimal corrosion on 304 (Fig. S7).

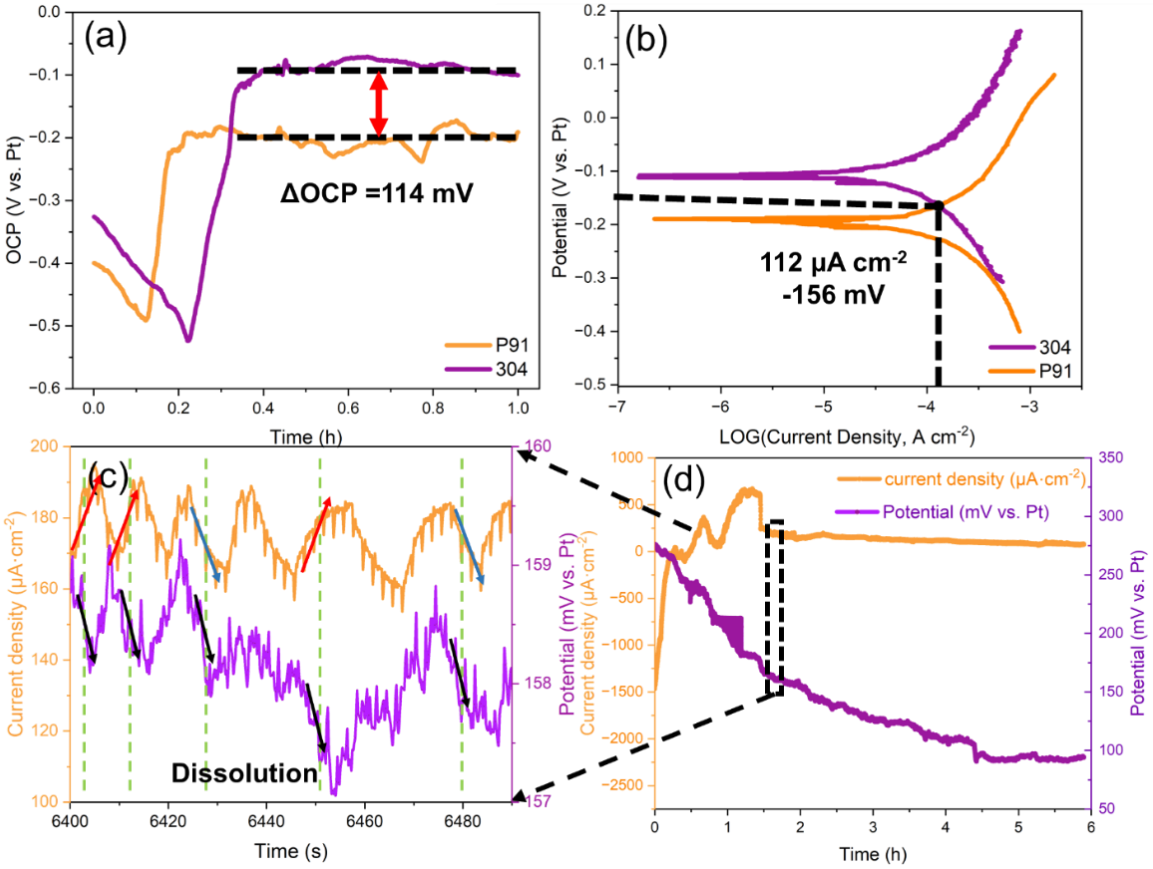

Fig. 10 The electrochemical test results of P91 and 304 base metals machined from GCTJ in molten salts at 700°C: (a) OCP curves, the average difference (△OCP) between 304 and P91 is calculated; (b) PDP curves, highlighting the intersection point where current density and potential are marked; (c) 90 s trace of potential and current transients from 6400 s after immersion in molten salts. The black downward arrows marked on the potential curve represent the dissolution events of electrodes. The red upward arrows on the current density curve suggest the anodic dissolution while the blue downward arrows indicate the cathodic dissolution; (d) The 6 h profile of current density and potential curves measured by ZRA technique for galvanically-coupled P91/304 electrodes in molten salts at 700°C.

Table 2 Electrochemical parameters obtained by Tafel linear fitting of the polarization curves for 304 and P91 in the molten salts at 700°C.

Alloy	E_{corr}	β_a	β_c	I_g	E_g
304	-108 mV	149 mV dec^{-1}	174 mV dec^{-1}	112 μA cm^{-2}	-156 mV
P91	-202 mV	180 mV dec^{-1}	137 dec^{-1}		

4. Discussion

4.1 Microstructure Effect on GCTJ

The present study reveals the presence of a distinct dual-phase microstructure of ferrite and tempered martensite within the P91 triangle zone. The ferrite formation is attributed to diffusion processes occurring during the hot isostatic pressing (HIP) process, as shown in Fig. S1b. Primarily, Chromium (Cr) and Nickel (Ni) diffuse from the 304 side, while carbon (C) migrates from the P91 side at elevated temperatures. The enrichment of Cr and depletion of C within the P91 triangle promote the formation of ferrite, as supported by previous studies [28,29].

The corrosion susceptibility of these two phases within the P91 triangle differs during the initial stage of corrosion. Compared with ferrite, tempered martensite is prone to pitting initiation. The initial corrosion behavior of the P91 triangle is influenced by its dual-phase microstructure through three primary factors: Cr content, precipitation, and dislocation density [42]. The Cr which stabilizes the ferrite phase, is approximately 10 wt% within the ferrite, compared to 8.5 wt% in the tempered martensite, as shown in Fig. 11a and Fig. 11b. Cr is dissolved into the ferrite uniformly, whereas Cr enriched precipitates are formed within tempered martensite (Fig. 11c and Fig. 11d). These Cr enriched precipitates are identified as carbides in the form of M23C6, as shown in Fig. S11. The formation of these carbides would consume the Cr, leading to local depletion of Cr in their vicinity [43,44], which can significantly affect corrosion behavior. The SKPFM results (Fig. 5) demonstrate that the largest localized Volta potential differences occur between the carbides and the surrounding matrix within the tempered martensite. The surrounding zones with reduced Volta potential, indicative of Cr depletion, are more prone to preferential dissolution in molten salt environments [42,45,46]. Additionally, high-energy crystal defects, such as dislocations (as shown in Fig. 3) within tempered martensite serve as precursors for corrosion initiation [33]. As a result, tempered martensite decorated with precipitates exhibits a greater vulnerability to pitting initiation.

Despite this, the similar Volta potential between ferrite and tempered martensite indicates that the overall corrosion resistance of these two phases is comparable. In the prolonged

corrosion exposure, both ferrite and tempered martensite are corroded within the P91 triangle, as shown in Fig. 8.

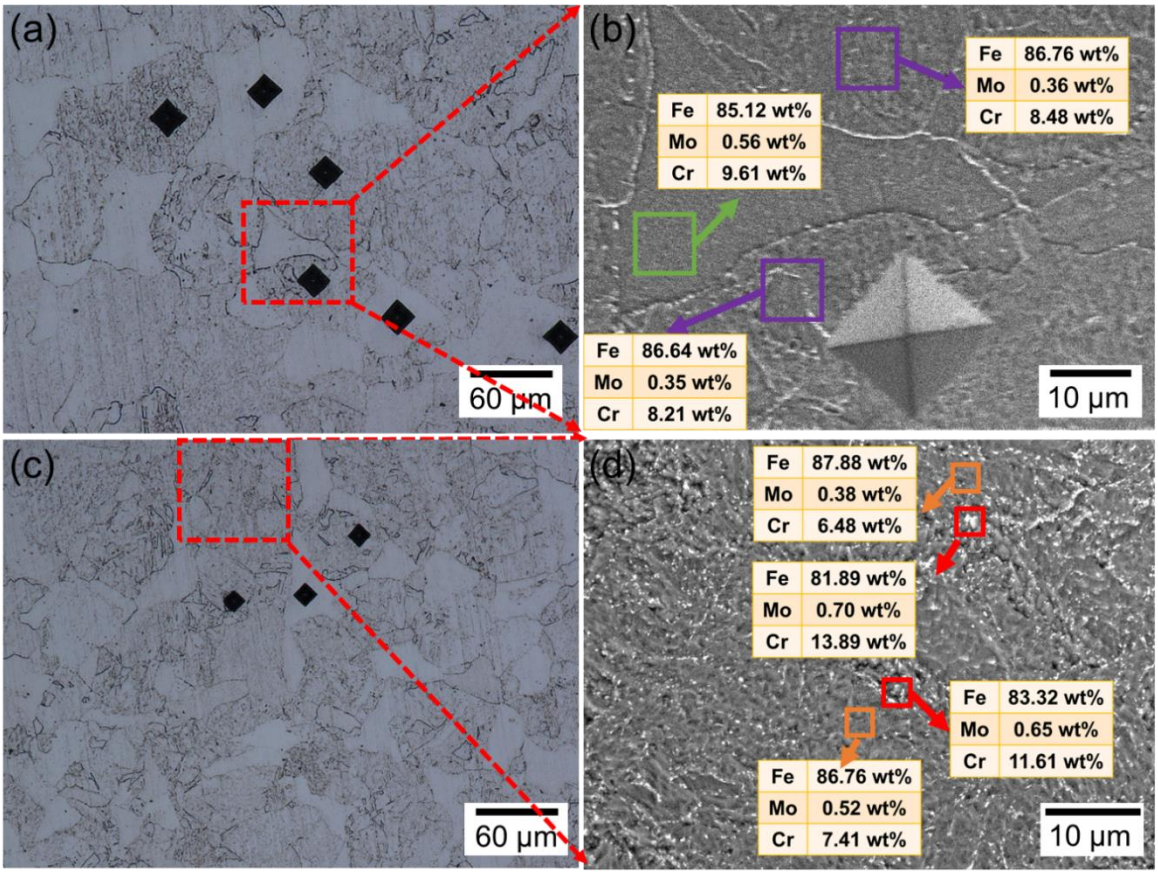

Fig. 11 (a) and (c) The OM image showing the ferrite and tempered martensite after the hardness test; (b) and (d) The SEM figure of selected areas from (a) and (c), respectively. The elemental content of the surface identified by EDS in different zones is marked in the figure.

4.2 Effect of Electrochemical surface area ratio

The galvanic corrosion is inevitable at the interface of dissimilar metals. However, the prolonged corrosion behavior of GCTJ is significantly different from that of DMW. The corroded morphologies of DMW after 1 h and 5 h are shown in Fig. S9, where the corrosion depth observed along the y-axis at the interface between P91 and ER309 is relatively consistent. In contrast, GCTJ exhibits a gradient corrosion degradation along the y-axis (Fig. 7 and Fig. 8), which is attributed to the novel joining configuration of the dissimilar metals. Electrochemical test results (Fig. 10) indicate that 304 stainless steel, with a more positive corrosion potential, acts as the cathode, while P91 steel functions as

the anode in the galvanic couple. To elucidate this relationship, the ratio Sc/Sa is introduced, where Sc represents the exposed surface area of the cathodic material and Sa denotes that of the anodic material. In the context of DMWs, ER309 serves as the cathode due to its higher nobility compared to P91 steel. As illustrated in Fig. 12a, the GCTJ presents a gradient in the Sc/Sa ratio along the y-axis, whereas the DMW maintains a fixed 1:1 ratio. The degradation depth of GCTJ and DMW after the 1 h and 5 h tests is summarized in Fig. 12b. As can be seen, the corrosion depth of GCTJ increases along with the rising Sc/Sa in the range of 0.6-5.3, reaching an average 9.5 μm (after 1 h corrosion) and 41.2 μm (after 5 h corrosion), significantly deeper than that on DMW (6.9 μm after 1 h corrosion and 15.9 μm after 5 h corrosion). Beyond a Sc/Sa ratio of 5.3, the degradation depth of both 1 h corroded GCTJ and 5 h corroded GCTJ is reduced. This enhanced corrosion resistance at the P91 triangle tip is likely due to the higher content of Cr and Ni (10.6 wt%Cr, 0.8 wt%Ni) than that of P91 base metal (9.2 wt%Cr, 0.1 wt%Ni), as shown in Fig. S10 [47]. Despite the improved resistance, the P91 triangle tip still exhibits greater corrosion depth than that observed in DMW.

The gradient corrosion severity of GCTJ underscores the dominant influence of the Sc/Sa in the prolonged corrosion test. To further evaluate the effect of electrochemical surface area ratio in the galvanic corrosion of GCTJ, the electrochemical noise test was conducted on 304/P91 couples with a series of Sc/Sa. Fig. 12c displays the time dependence of the galvanic current density for the 304/P91 couple in molten salts. The average I_g of 304/P91 couples with a series of Sc/Sa is calculated in Fig. 12d. The I_g increases with the rising exposed surface area ratio between 304 and P91, indicating that galvanic corrosion becomes more pronounced in regions where 304 occupies a larger area relative to P91.

To further understand the mechanism of galvanic coupling in accelerating the corrosion rate, a quantitative relation between the dissolution current density of P91 and Sc/Sa is now discussed. The anodic dissolution current density, I_a was calculated from Equation 1 and presented in Fig. 12d [41].

$$\frac{I_g}{I_a} = 1 - \exp\left(-\frac{2.303(\beta_c+\beta_a)(E_g-E_{corr})}{\beta_c\beta_a}\right) \quad (1)$$

Where β_a and β_c represent the anodic and cathodic Tafel constants of P91, E_{corr} is the corrosion potential of P91, and the I_g is the average galvanic current density obtained from Fig. 12c. The I_a can be estimated from the values of I_g and E_g.

Table 3 The average I_g and I_a were calculated according to the galvanic current density for the 304/P91 couple with different Sc/Sa.

Sc:Sa	2:3	1:1	4:1
I_g (μA cm^{-2})	17.53	108.53	318.50
I_a (μA cm^{-2})	23.57	145.91	428.20

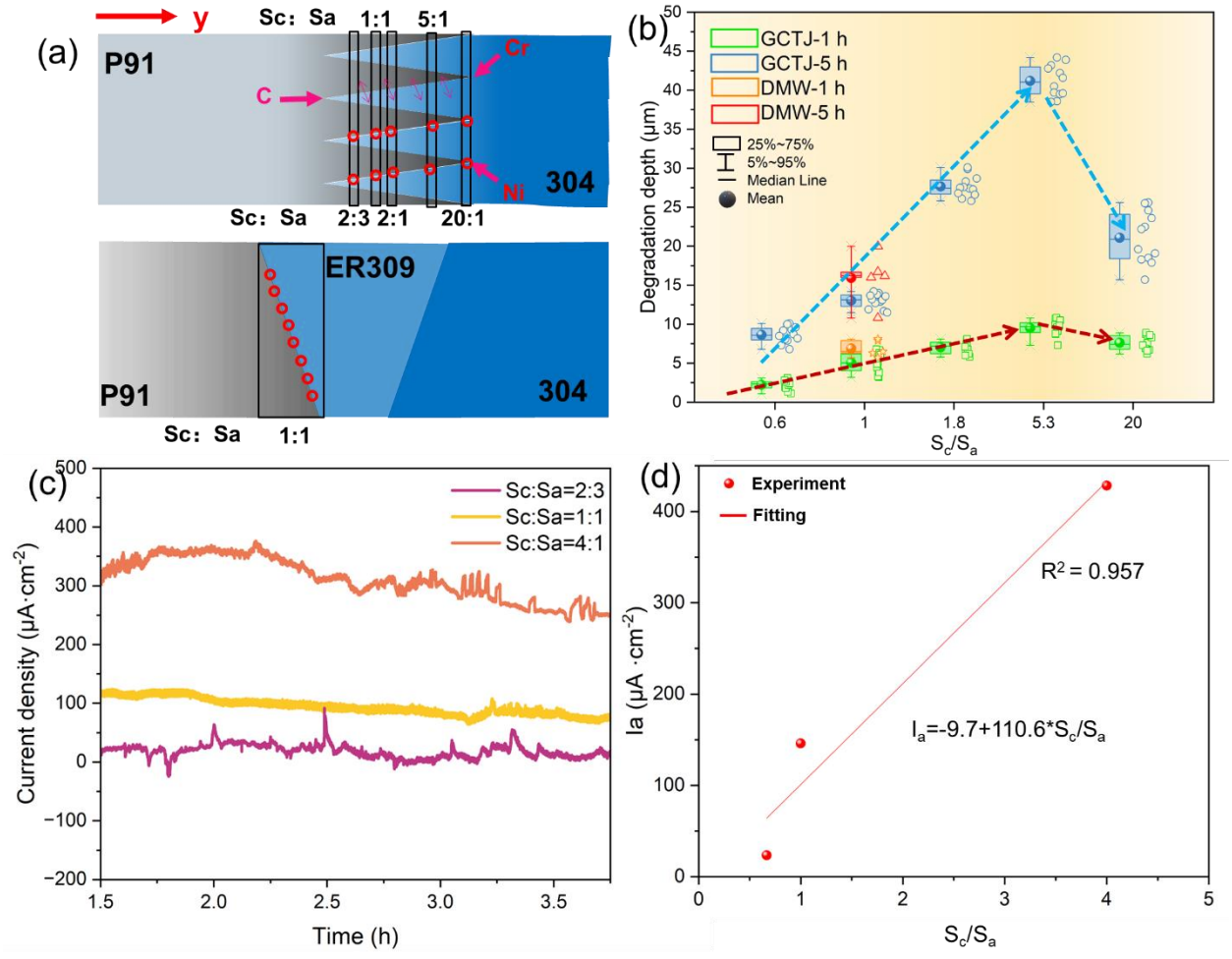

Fig. 12 (a) The joining configuration of GCTJ and DMW; (b) The degradation depth is summarized from the red circle in (a). The boxplot illustrates the degradation depth variation along the Sc/Sa; (c) Time dependence of the galvanic current density for a 304/P91 couple measured by ZRA technique in molten salts at 700°C with different Sc/Sa; (d) The effect of Sc/Sa on anodic dissolution current density of P91 in the molten salts at 700°C.

Based on the electrochemical parameters in Table 2, the average Ia representing the galvanic effect of 304 on the corrosion of P91 is calculated in Table 3. As shown in Fig. 12d, during the testing hours, the average I_a linearly increases with the increasing Sc/Sa, demonstrating that the accelerating galvanic effect by Sc/Sa is linearly related to the corrosion rate of P91 in molten salts [41]. This linear accelerated corrosion effect is manifested in the gradient change of the degradation depth along the P91 triangle (Fig. 12b). To minimize the severe localized corrosion in the transition zone, the exposure of the surface of the P91 top triangle zone to combustion should be avoided as much as possible.

4.3 Hot Corrosion Mechanism

The mechanism of the hot corrosion caused by molten sulfate salts at elevated temperatures has been thoroughly investigated by previous studies [48,49]. The initially deposited solid salts turn to a molten layer when the joint coupons are exposed to 700°C [26]. This molten layer acts as an ionic conductor [50], triggering the electrochemical degradation of the active elements, as shown in 9)

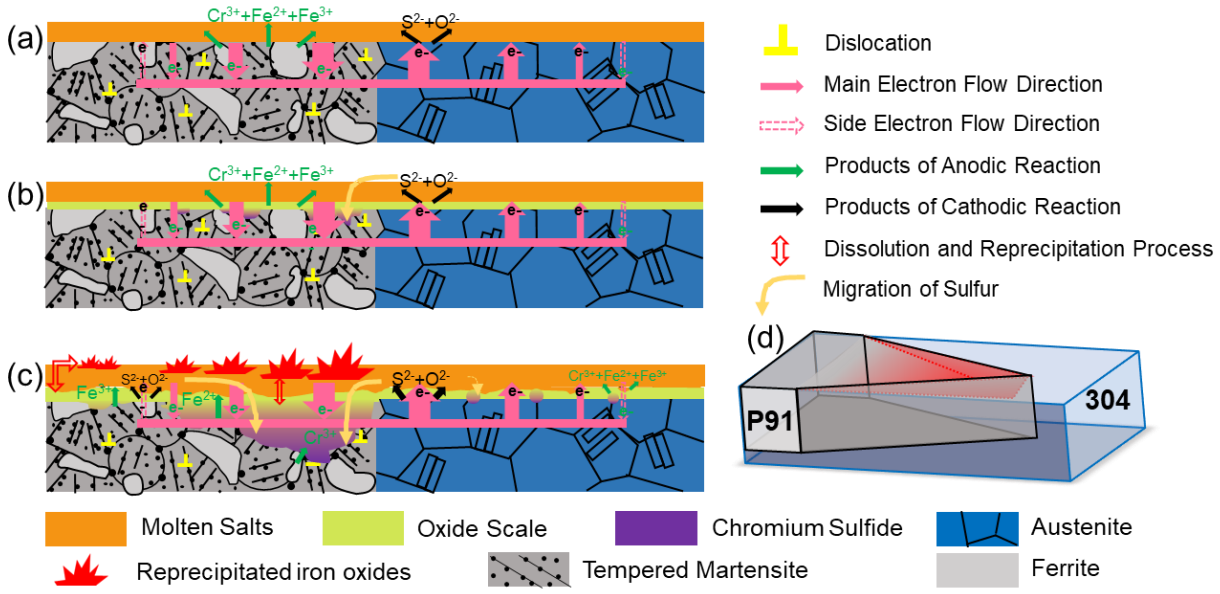

Fig. *13* a. The direction of electron flow is indicated at the interface of 304 and P91 by the solid pink arrows, and its width is designated for the extent of the galvanic coupling. At the onset of hot corrosion, the sulfate ions in the molten layer dissociate according to Equation 2 [49,51,52]. Primary anodic reactions (Equations 3–5) occur on the P91 side, while

cathodic reactions involving the reduction of SO_3 (Equations 6) and O_2 (O_2 in atmosphere can be dissolved in the molten layer according to Equation 7 and then be reduced in Equation 8 [50,53]) predominantly occur on the 304 side. During the early stages of corrosion, the initial corrosion attacks under molten salts mainly occur within tempered martensite due to more vulnerable sites (localized Cr-depleted zones and crystal defects), as shown in 9)

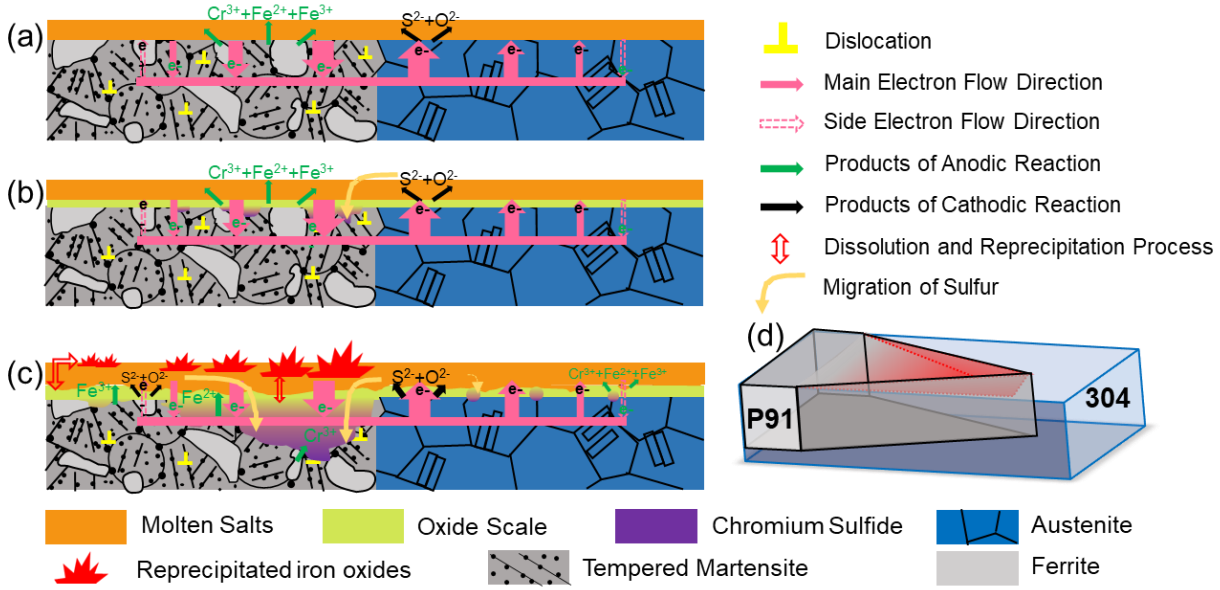

Fig. *13* b. The Ellingham diagram for the oxidation and sulfidation products is calculated in Fig. S12. At the molten salt/metal interface, an oxide scale is initially formed due to the affinity of cations bonding with oxygen rather than sulfur [25], mainly in iron oxides and a few chromium oxides. Considering the higher diffusion coefficient of iron compared to any other alloying elements in the oxide scale, the oxide scale grows by forming more iron oxides [54]. Due to limited oxygen diffusion through thick oxide layers, at the metal/oxide interface, a reduction in the oxygen partial pressure is often observed [55]. Under these conditions, the affinity of Cr for sulfur is enhanced. Consequently, instead of forming Cr_2O_3, Cr reacts with the incoming sulfur to form chromium sulfide [56]. This phenomenon is particularly pronounced in environments characterized by a high sulfur availability and reduced oxygen partial pressure [51].

As the exposure time increases (as shown in 9)

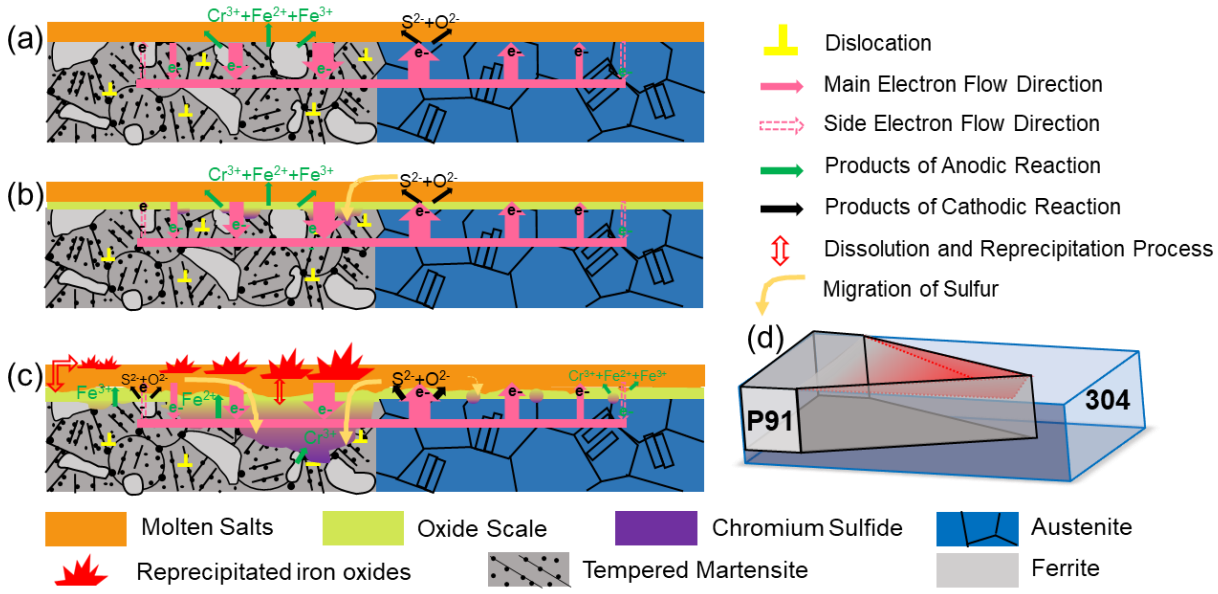

Fig. *13* c), both ferrite and tempered martensite within P91 are corroded since the corrosion resistance of these two phases is similar, as reflected by the average Volta potential (Fig. 5). The removal of sulfur by forming sulfidation products will increase local basicity (in the form of Na_2O) in the molten salt layer [53,57]. As a result, the oxide scale will dissolve and reprecipitate as non-protective oxides at the molten salts/gas interface, as described in Equation 9 [58,59]. The porous iron oxide reprecipitation can further facilitate the capture and entry of oxygen and sulfur into the steel matrix [25,60], leading to more severe corrosion attacks.

Notably, the corrosion depth is reduced from the top to the bottom of the P91 triangle in the transition zone, as shown in 9)

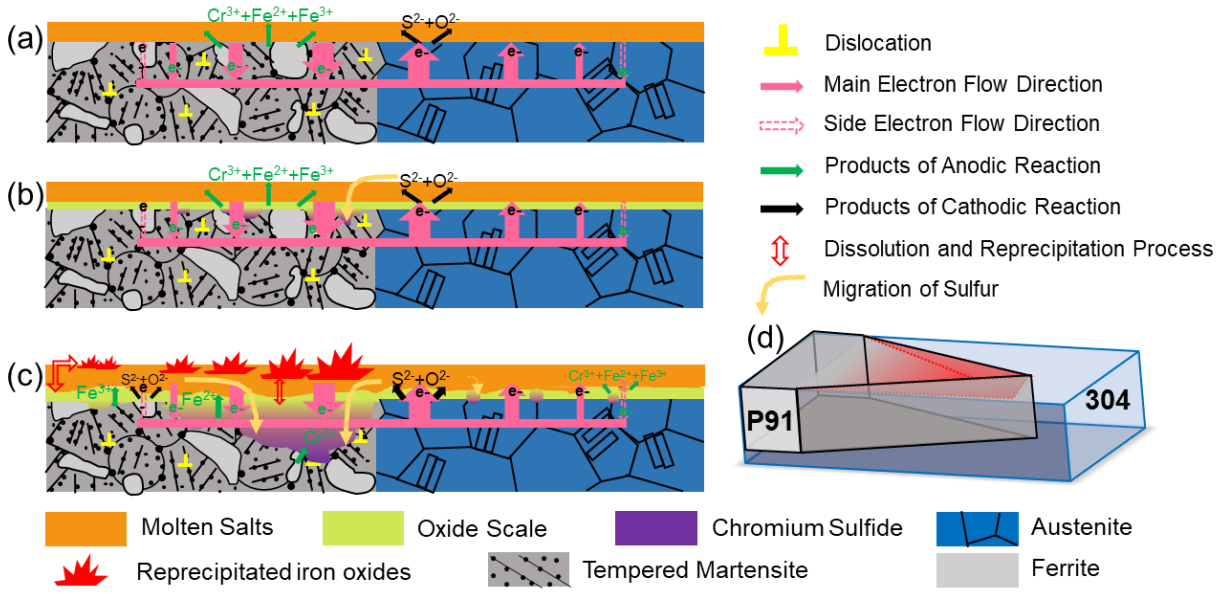

Fig. 13d. This gradient degradation indicates that the galvanic couple's acceleration effect is dominant in the hot corrosion process of the transition zone, especially on the top zone of the P91 triangle. Consequently, a critical concern for the structural integrity of this transient joint under corrosive and stressful conditions arises since these localized deep corrosion defects may significantly impair the mechanical properties of the joints [61].

$$SO_4^{2-} \rightarrow SO_3 + O^{2-} \quad (2)$$

$$Fe \rightarrow Fe^{2+} + 2e^- \quad (3)$$

$$Fe \rightarrow Fe^{3+} + 3e^- \quad (4)$$

$$Cr \rightarrow Cr^{3+} + 3e^- \quad (5)$$

$$SO_3 + 8e^- \rightarrow S^{2-} + 3O^{2-} \quad (6)$$

$$O_2 + 2O^{2-} \rightarrow 2O_2^{2-} \quad (7)$$

$$O_2^{2-} + 2e^- \rightarrow 2O^{2-} \quad (8)$$

$$Fe_2O_3 + O^{2-} \leftrightarrow 2FeO_2^- \quad (9)$$

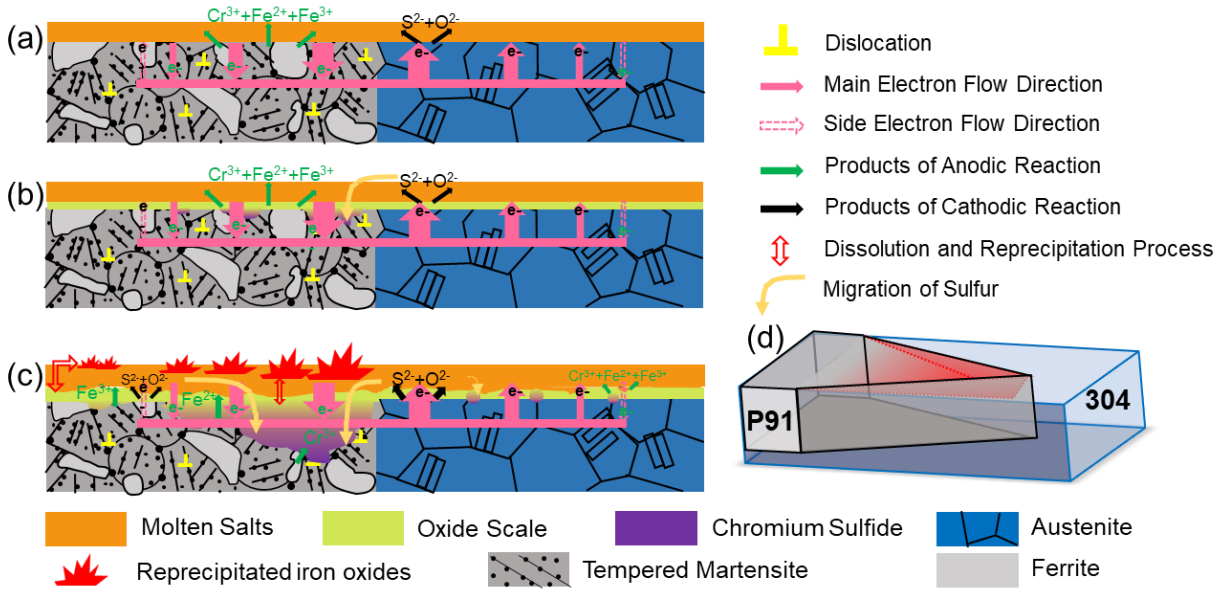

Fig. 13 The schematic diagram illustrates the hot corrosion mechanism of the GCTJ exposed to molten salts: (a) The deposited salts become molten and trigger hot corrosion. (b) During the early stage of corrosion, the initial corrosion attacks under molten salts mainly occur within tempered martensite. (c) With prolonged exposure, the corrosion attacks happen on both ferrite and tempered martensite. (d) The gradient corrosion depth within the P91 triangle.

5. Conclusion

In this study, the corrosion behavior of GCTJ was investigated under simulated salt deposition (50at% Na_2SO_4 and 50at% $MgSO_4$) at 700°C. Corrosion within the dissimilar joining zone is more pronounced on P91 than on 304. Specifically, GCTJ exhibits significantly deeper degradation compared to DMW under the same condition, with the most severe corrosion occurring on the top zone of the P91 triangle, leading to potential stress concentrations and crack initiation. At the onset of corrosion, the pitting initiation is affected by the dual-phase microstructure. Anodic dissolution mainly occurs within the tempered martensite due to more vulnerable sites within the tempered martensite. However, with prolonged exposure, ferrite and tempered martensite are corroded within the P91 triangle due to their comparable Volta potentials. The corrosion depth increases as the exposed surface area ratio between 304 and P91 rises. Electrochemical analysis demonstrates galvanic corrosion between 304 and P91, where the anodic dissolution current density (I_a) scales linearly with the Sc/Sa in molten salts, highlighting the effect of

electrochemical surface area ratio in the corrosion severity of GCTJ. These findings provide preliminary insights into GCTJ corrosion behavior, offering guidance for mitigating corrosion-induced degradation, and advancing the design and manufacturing of next-generation transition joints to improve service performance.

CRediT authorship contribution statement

Ting Sun: Conceptualization, Methodology, Investigation, Validation, Formal analysis, Data curation, Writing – original draft, Writing – review and editing. **Shanshan Hu:** Supervision, Conceptualization, Methodology, Project administration, Writing – review and editing. **Alexander I. Ikeuba:** Writing – review and editing. **Yuying Wen:** Investigation, Review and Editing. **Xingru Tan:** Investigation, Review and editing. **Youyuan Zhang:** Review and methodology of electrochemical test. **Haiyang Qian**: Conception, Review and Edition. **Yanli Wang:** Conception, Review and editing. **Zhili Feng:** Conception, Review and editing. **Bai Cui:** Conception, Review and editing. **Xingbo Liu:** Supervision, Conceptualization, funding acquisition, Supervision, Project administration, Writing – review and editing.

Declaration of competing interest

X.L., H.Q., Y.W., and Z.F. report to a patent application regarding the GCTJ.

Data Availablity

Data will be made available on request.

Acknowledgments

This investigation was funded by the U.S. Department of Energy under contract number DE-FE-0031819. The authors thank their partners at ORGL, GE, and UNL for their technical guidance and financial support.

Reference

1. Zhang, X., Tu, S.-T. & Xuan, F. Creep–fatigue endurance of 304 stainless steels. *Theoretical and Applied Fracture Mechanics* **71**, 51–66 (2014).
2. Carrizo, D. A., Besoky, J. I., Luppo, M., Danon, C. & Ramos, C. P. Characterization of an ASTM A335 P91 ferritic-martensitic steel after continuous cooling cycles at moderate rates. *Journal of Materials Research and Technology* **8**, 923–934 (2019).
3. Zhou, H. *et al.* Significant reduction in creep life of P91 steam pipe elbow caused by an aberrant microstructure after short-term service. *Sci Rep* **14**, 5216 (2024).
4. Sirohi, S., Pandey, C. & Goyal, A. Role of the Ni-based filler (IN625) and heat-treatment on the mechanical performance of the GTA welded dissimilar joint of P91 and SS304H steel. *Journal of Manufacturing Processes* **65**, 174–189 (2021).
5. Sharma, P. & Dwivedi, D. K. A-TIG welding of dissimilar P92 steel and 304H austenitic stainless steel: Mechanisms, microstructure and mechanical properties. *Journal of Manufacturing Processes* **44**, 166–178 (2019).
6. Akram, J., Kalvala, P. R., Misra, M. & Charit, I. Creep behavior of dissimilar metal weld joints between P91 and AISI 304. *Materials Science and Engineering: A* **688**, 396–406 (2017).
7. Subramanian, M. *et al.* Heterogeneous creep deformation in Dissimilar Metal Welds (DMWs). *Materials Science and Engineering: A* **749**, 1–13 (2019).
8. Zhang, Y. *et al.* Effect of nickel-based filler metal types on creep properties of dissimilar metal welds between Inconel 617B and 10% Cr martensitic steel. *Journal of Materials Research and Technology* **14**, 2289–2301 (2021).

9. Francis, J. A., Mazur, W. & Bhadeshia, H. K. D. H. Review Type IV cracking in ferritic power plant steels. *Materials Science and Technology* **22**, 1387–1395 (2006).
10. Tabuchi, M., Hongo, H. & Abe, F. Creep Strength of Dissimilar Welded Joints Using High B-9Cr Steel for Advanced USC Boiler. *Metall and Mat Trans A* **45**, 5068–5075 (2014).
11. Liu, X. *et al. Additively Manufactured Graded Composite Transition Joints (AM-GCTJ) for Dissimilar Metal Weldments in Advanced Ultra-Supercritical Power Plant*. (2020).
12. Liu, X. *et al. Additively Manufactured Graded Composite Transition Joints (AM-GCTJ) for Dissimilar Metal Weldments in Advanced Ultra-Supercritical Power Plant*. (2021).
13. DebRoy, T. *et al.* Additive manufacturing of metallic components – Process, structure and properties. *Progress in Materials Science* **92**, 112–224 (2018).
14. Zuback, J. S., Palmer, T. A. & DebRoy, T. Additive manufacturing of functionally graded transition joints between ferritic and austenitic alloys. *Journal of Alloys and Compounds* **770**, 995–1003 (2019).
15. DuPont, J., Babu, S. & Feng, Z. *Development of Novel Functionally Graded Transition Joints for Improving the Creep Strength of Dissimilar Metal Welds in Nuclear Applications*. 1461179 (2018) doi:10.2172/1461179.
16. Homaeian, A. & Alizadeh, M. Interaction of hot corrosion and creep in Alloy 617. *Engineering Failure Analysis* **66**, 373–384 (2016).

17. Fetni, S., Toumi, A., Mkaouar, I., Boubahri, C. & Briki, J. Microstructure evolution and corrosion behaviour of an ASTM A213 T91 tube after long term creep exposure. *Engineering Failure Analysis* **79**, 575–591 (2017).
18. Task, M. N., Gleeson, B., Pettit, F. S. & Meier, G. H. Compositional effects on the type I hot corrosion of β-NiAl alloys. *Surface and Coatings Technology* **206**, 1552–1557 (2011).
19. Gleeson, B. High-temperature corrosion of metallic alloys and coatings. in *Materials Science and Technology: A Comprehensive Treatment* (eds. Cahn, R. W., Haasen, P. & Kramer, E. J.) 173–228 (Wiley, 2000). doi:10.1002/9783527619306.ch14.
20. Arivazhagan, N., Singh, S., Prakash, S. & Reddy, G. M. Hot corrosion studies on dissimilar friction welded low alloy steel and austenitic stainless steel under chlorine containing salt deposits under cyclic conditions. *Corrosion Engineering, Science and Technology* **44**, 369–380 (2009).
21. Kim, S.-W., Kim, D.-J. & Kim, H.-P. Evaluation of Galvanic Corrosion Behavior of SA-508 Low Alloy Steel and Type 309L Stainless Steel Cladding of Reactor Pressure Vessel under Simulated Primary Water Environment. *Nuclear Engineering and Technology* **44**, 773–780 (2012).
22. Okonkwo, B. O. *et al.* Galvanic corrosion study between low alloy steel A508 and 309/308 L stainless steel dissimilar metals: A case study of the effects of oxide film and exposure time. *Journal of Nuclear Materials* **548**, 152853 (2021).
23. Cerit, M., Genel, K. & Eksi, S. Numerical investigation on stress concentration of corrosion pit. *Engineering Failure Analysis* **16**, 2467–2472 (2009).

24. Jie, Z., Li, Y., Wei, X. & Zhuge, P. Fatigue life prediction of welded joints with artificial corrosion pits based on continuum damage mechanics. *Journal of Constructional Steel Research* **148**, 542–550 (2018).
25. Buscaglia, V., Nanni, P. & Bottino, C. The mechanism of sodium sulphate-induced low temperature hot corrosion of pure iron. *Corrosion Science* **30**, 327–349 (1990).
26. Nesbitt, J. & Draper, S. Pit morphology and depth after low-temperature hot corrosion of a disc alloy. *Materials at High Temperatures* **33**, 501–516 (2016).
27. Krielaart, G. P., Sietsma, J. & Van Der Zwaag, S. Ferrite formation in Fe-C alloys during austenite decomposition under non-equilibrium interface conditions. *Materials Science and Engineering: A* **237**, 216–223 (1997).
28. Bhadeshia, H. K. D. H. Diffusional formation of ferrite in iron and its alloys. *Progress in Materials Science* **29**, 321–386 (1985).
29. Sreepriya, T., Mythili, R. & Prasad Reddy, G. V. Correlation between microstructure and nanomechanical properties of 9Cr– 1Mo ferritic martensitic steel through instrumented indentation technique. *Materials Science and Engineering: A* **840**, 142985 (2022).
30. Singh, J. & Nath, S. K. Dissolution of delta ferrite through cyclic treatment and its influence on the hydro abrasive erosion and mechanisms. *Tribology International* **161**, 107056 (2021).
31. Li, J., Cheng, L., Zhang, P., Wang, L. & Li, H. Effect of delta ferrites on the anisotropy of impact toughness in martensitic heat-resistant steel. *Journal of Materials Research and Technology* **8**, 1781–1788 (2019).

32. Ji, D., Zhang, M., Zhu, D., Luo, S. & Li, L. Influence of microstructure and pre-straining on the bake hardening response for ferrite-martensite dual-phase steels of different grades. *Materials Science and Engineering: A* **708**, 129–141 (2017).
33. Chen, H., Lv, Z., Lu, L., Huang, Y. & Li, X. Correlation of micro-galvanic corrosion behavior with corrosion rate in the initial corrosion process of dual phase steel. *Journal of Materials Research and Technology* **15**, 3310–3320 (2021).
34. Revilla, R. I. Methods—On the Application of Ambient Scanning Kelvin Probe Force Microscopy to Understand Micro-Galvanic Corrosion Phenomena: Interpretation and Challenges. *Journal of The Electrochemical Society* **170**, 011501 (2023).
35. Song, D. *et al.* Corrosion behavior and mechanism of Cr-Mo alloyed steel: Role of ferrite/bainite duplex microstructure. *Journal of Alloys and Compounds* **809**, 151787 (2019).
36. Chen, H., Lu, L., Huang, Y. & Li, X. Insight into TiN inclusion induced pit corrosion of interstitial free steel exposed to aerated NaCl solution. *Journal of Materials Research and Technology* **13**, 13–24 (2021).
37. Soltanattar, S., Nowakowski, P., Bonifacio, C. S., Fischione, P. & Gleeson, B. Use of microanalysis to better understand the high-temperature corrosion behavior of chromium exposed to multi-oxidant environments. *Oxid Met* **91**, 11–31 (2019).
38. Gleeson, B. & Li, B. T. Cyclic oxidation of chromia-scale forming alloys: Lifetime prediction and accounting for the effects of major and minor alloying additions. *MSF* **461–464**, 427–438 (2004).

39. Rao, Ch. J., Venkatesh, P. & Ningshen, S. Corrosion assessment of 9Cr-1Mo steel in molten LiCl-KCl eutectic salt by electrochemical methods. *Journal of Nuclear Materials* **514**, 114–122 (2019).
40. Mohammadi Zahrani, E. & Alfantazi, A. M. High temperature corrosion and electrochemical behavior of INCONEL 625 weld overlay in PbSO4–Pb3O4–PbCl2–CdO–ZnO molten salt medium. *Corrosion Science* **85**, 60–76 (2014).
41. Qiu, J. *et al.* Galvanic corrosion of Type 316L stainless steel and Graphite in molten fluoride salt. *Corrosion Science* **170**, 108677 (2020).
42. Carvalho, R. N., Rincon Troconis, B. C., Pioszak, G., Ynciarte, V. & Scully, J. R. Effect of microstructure on the pitting susceptibility of a martensitic-ferritic stainless steel: A corrosion-metallurgical study. *Corrosion Science* **202**, 110277 (2022).
43. Pandey, C., Giri, A. & Mahapatra, M. M. Evolution of phases in P91 steel in various heat treatment conditions and their effect on microstructure stability and mechanical properties. *Materials Science and Engineering: A* **664**, 58–74 (2016).
44. Huang, X., Wang, D. & Yang, Y. Effect of Precipitation on Intergranular Corrosion Resistance of 430 Ferritic Stainless Steel. *Journal of Iron and Steel Research International* **22**, 1062–1068 (2015).
45. Clark, R. N., Searle, J., Martin, T. L., Walters, W. S. & Williams, G. The role of niobium carbides in the localised corrosion initiation of 20Cr-25Ni-Nb advanced gas-cooled reactor fuel cladding. *Corrosion Science* **165**, 108365 (2020).
46. Hou, Z., Babu, R. P., Hedström, P. & Odqvist, J. Microstructure evolution during tempering of martensitic Fe–C–Cr alloys at 700°C. *Journal of Materials Science* **53**, 6939–6950 (2018).

47. Li, K. & Zeng, Y. Corrosion of heat exchanger materials in co-combustion thermal power plants. *Renewable and Sustainable Energy Reviews* **161**, 112328 (2022).
48. Birks, N., Meier, G. H. & Pettit, F. S. *Introduction to the High Temperature Oxidation of Metals*. (Cambridge University Press, 2006).
49. Young, D. J. *High Temperature Oxidation and Corrosion of Metals*. vol. 1 (Elsevier, 2008).
50. Wang, X. H. & Zhou, Y. C. Hot Corrosion of Na2SO4-Coated Ti3AlC2 in Air at 700-1000°C. *Journal of The Electrochemical Society* **151**, B505 (2004).
51. Li, L. *et al.* AlxCoCrFeNi high entropy alloys with superior hot corrosion resistance to Na2SO4 + 25% NaCl at 900 °C. *Corrosion Science* **187**, 109479 (2021).
52. Goebel, J. A. & Pettit, F. S. Na2SO4 Induced Accelerated Oxidation (Hot Corrosion) of Nickel. *Metallurgical Transactions* **1**, 1943–1954 (1970).
53. Shi, L. Accelerated Oxidation of Iron Induced by Na2SO4 Deposits in Oxygen at 750C—New Type Low- Temperature Hot Corrosion. *Oxidation of Metals* **40**, 197–211.
54. Persdotter, A., Eklund, J., Liske, J. & Jonsson, T. Beyond breakaway corrosion – Influence of chromium, nickel and aluminum on corrosion of iron-based alloys at 600 ° C. *Corrosion Science* **177**, 108961 (2020).
55. Wu, X. High-temperature corrosion behavior of alloys in gaseous enviroments with low-oxygen and high-sulfur potentials.
56. Gleeson, B. Alloy degradation under oxidizing-sulfidizing conditions at elevated temperatures. *Mat. Res.* **7**, 61–69 (2004).

57. Rapp, R. Chemistry and Electrochemistry of the Hot Corrosion of Metals. *Corrosion (Houston, Tex.)* **42**, 568–577 (1986).
58. Rapp, R. A. Hot corrosion of materials: a fluxing mechanism? *Corrosion Science* **44**, 209–221.
59. Rapp, R. A. & Zhang, Y.-S. Hot corrosion of materials: Fundamental studies. *JOM* **46**, 47–55 (1994).
60. Dlugosch, T. *et al.* Thermal oxidation synthesis of crystalline iron-oxide nanowires on low-cost steel substrates for solar water splitting. *Semicond. Sci. Technol.* **32**, 084001 (2017).
61. Songbo, R. *et al.* Effects of the corrosion pitting parameters on the mechanical properties of corroded steel. *Construction and Building Materials* **272**, 121941 (2021).